Lab on a Chip

Accepted Manuscript

ROYAL SOCIETY OF CHEMISTRY

www.rsc.org/loc

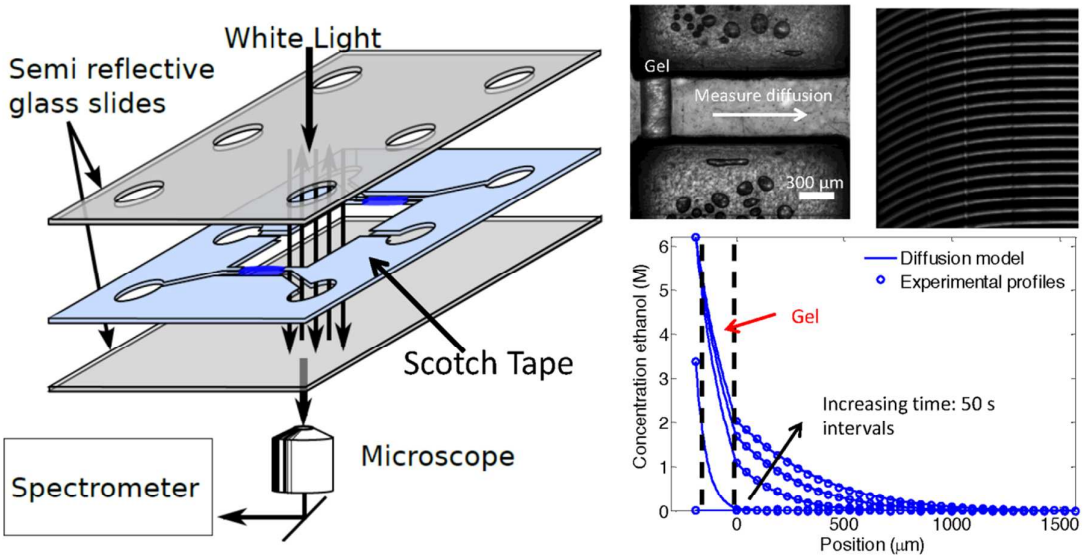

We developed a simple, Fabry-Perot interferometric technique, which allows for the measurement of concentration profiles *in situ* without any chemical label. The technique is used to quickly measure diffusion coefficients.

ARTICLE TYPE www. rsc.org/xxxxxx | XXXXXXXX

Measuring concentration fields in microfluidic channels *in situ* with a Fabry-Perot interferometer

Douglas R. Vogus†, Vincent Mansard†, Michael V. Rapp, and Todd M. Squires*

Received Xth XXXXXXXXXX 20XX, Accepted Xth XXXXXXXXX 20XX
First published on the web Xth XXXXXXXXXX 200X
DOI: 10.1039/b000000x

Recent advancements in microfluidic technology have allowed for the generation and control of complex chemical gradients; however, few general techniques can measure these spatio-temporal concentration profiles without fluorescent labeling. Here we describe a Fabry-Perot interferometric technique, capable of measuring concentration profiles *in situ*, without any chemical label, by tracking *Fringes of Equal Chromatic Order* (FECO). The technique has a sensitivity of 10^{-5} RIU, which can be used to track local solute changes of $\sim$0.05% (w/w). The technique is spatially resolved (1 μm) and easily measures evolving concentration fields with $\sim$20 Hz rate. Here, we demonstrate by measuring the binary diffusion coefficients of various solutes and solvents (and their concentration-dependence) in both free solution and in polyethylene glycol diacrylate (PEG-DA) hydrogels.

1 Introduction

The field of microfluidics continues to grow as novel microfluidic tools are developed, offering solutions to a broad range of scientific and technical problems and applications. Recent advances have enabled the rapid generation of complex chemical environments, such as well defined gradients (e.g. for fundamental chemotaxis studies and high throughput screens of chemical reaction conditions).[1–6] Unfortunately, few general methods exist to measure the dynamic chemical profiles *in situ* in microfluidic devices.

Many techniques have been developed to generate chemical gradients on the micro scale. One of the most common is to generate gradients with repeated T-junctions of miscible fluids.[7–9] Although the technique allows for the design of gradients with various shapes, drawbacks include the need to precisely control the pressure of each inlet stream and that the gradient is developed in laminar flow streams. Recently, new methods were developed to generate chemical gradients with diffusive transport, eliminating convection in the region of interest.[10–17] The technique entails having a microchip with a closed dialysis chamber (CDC), isolated from a source and sink channel by gel membranes that allow for solute diffusion. CDCs allow both fast chemical switching and rapid generation of complex chemical gradients due to small length scales.[11–13,17]

With continued advancements in microfluidic gradient generation, the need to measure these concentration fields *in situ* increases. For example, the dynamics involved in developing a chemical gradient in a CDC requires knowledge of the transport processes involved in the dialysis membranes and in the CDC, which will be species specific. A general method to measure concentration fields *in situ* would facilitate the quantification of transport processes in the exact experimental system. Moreover, many systems of scientific, industrial, and technological relevance involve time-dependent processes in which materials precipitate, crystallize, dissolve, react, or equilibrate. Such processes, in turn, involve spatio-temporally evolving concentration fields of solute and solvent. Unfortunately, there is a lack of reliable and general methods to measure spatial concentration profiles *in situ*.

In microfluidic systems, fluorescence microscopy is commonly used to measure the spatial concentration profile of chemicals. Although the technique is quick and easy to set up, chemicals must be tagged with a fluorophore, potentially affecting their function and transport properties; moreover, photo bleaching can lead to erroneous measurements. Other techniques have been adapted to microsystems, including Raman spectroscopy,[18–20] Fourier transform infrared (FT-IR) spectroscopy,[21] and Coherent Anti-Stokes Raman scattering (CARS) microscopy,[22] allowing for the spatial visualization of chemical species without fluorescent labeling. In particular, *Schafer et al* have resolved 3D concentration profiles with sub-μm resolution using CARS microscopy; however, minutes are required to resolve concentration gradients over $\sim 100\,\mu m$.[22] On the contrary, *Chan et al* resolved multiple chemical concentration profiles over multiple millimeters in seconds with FT-IR spectroscopy; however, the technique only has a lateral resolution of 40 μm.[21]

Refractive index measurements provide another strategy to measure concentration profiles. Various interferometric tech-

Department of Chemical Engineering University of California, Santa Barbara. E-mail: squires@engineering.ucsb.edu, † Authors contributed equally to this work

niques have been adapted to microfluidic systems to precisely measure the average refractive index of a single (as low as $\sim \mu m^3$) point in space, down to 10^{-4} to 10^{-7} RIU, including a mach-zender interferometer,[23] a back scattering interferometer,[24], a Young interferometer,[25] and Fabry-Perot interferometers.[26–28] To our knowledge, only one refractometry method, consisting of a Fabry-Perot interferometer with a monochromator, is able to resolve spatial refractive index profiles in a fluidic system.[29] This technique is optimized for measurements in nanofluidic channels and not immediately applicable to measuring evolving concentration profiles in microfluidic channels.

Here we demonstrate a Fabry-Perot interferometric system designed to measure the local concentration of chemical species in microchannels with or without flow. Fabrication of the Fabry-Perot chip is relatively simple, and the *Fringes of Equal Chromatic Order* (FECO) are generated directly on an inverted microscope and imaged with a spectrometer and CCD camera, enabling the technique to be easily utilized to study various transport processes in microfluidic devices. By following the displacement of the FECO fringes, we resolve changes in refractive index down to 2×10^{-5} RIU. A spatially resolved spectrometer enables the local refractive index to be measured with 1 μm resolution. The temporal resolution on each measurement is ~ 0.05s and is only limited by the sensitivity of the camera.

We first describe the fabrication of the interferometer and the experimental methods used to track the FECO fringes. We then discuss the spatial and temporal resolution and precision of the refractrometry method by looking at the concentration of chemicals in rectangular channels with homogenous concentrations. Lastly, we use the technique to measure the diffusive evolution of chemical gradients in microfluidic channels to measure binary diffusion coefficients and concentration dependence and to track the evolution of chemical gradients in CDCs.

2 Materials and methods

Here we describe the fabrication of the microfluidic interferometer chip, the acquisition of FECO fringes, and the image analysis used to determine refractive index as a function of space and time.

2.1 Microfluidic chip fabrication

A microfluidic device consisting of a single, 90 μm layer between semi-reflective glass surfaces was fabricated (Fig. 1). After drilling inlet holes into one of the glass slides, electron-beam evaporation (SEC600, CHA, Industries) was used to deposit a 5 nm adhesion layer of TiO_2 and 50 nm layer of Ag onto the glass slides to make them semi reflective. Oxidation

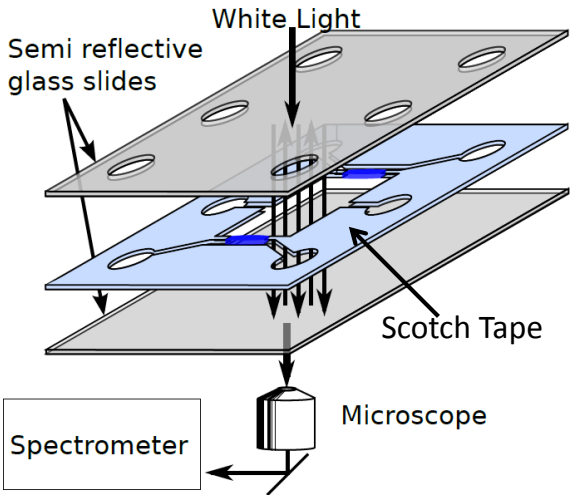

Fig. 1 Diagram of light path in microfluidic, Fabry-Perot interferometer.

of the silver layer (which can reduce the performance of the device due to a decrease in finesse) was observed over a few days; however, this can be delayed if a longer lifetime is desired by storing devices under vacuum when not in use or by depositing a protective SiO_2 layer.[29] Even with oxidation, devices still performed effectively weeks after fabrication.

A laser cutter (Trotec Speedy 100) was used to cut channels into the double sided tape (Permanent Double Sided Tape, Scotch), which was then sandwiched between the two glass slides by applying pressure. While the laser cutter allows for any tape design with feature sizes down to 100 μm, smaller features are possible with standard lithography techniques, if necessary. PDMS inlets were then ozone bonded to the top glass slide to hold inlet and outlet tubing. The device was then baked at 80°C for at least 4 hours to strengthen bonding.

2.2 Multiple beam FECO interferometry

FECO interferometry, which is used to simultaneously measure film thickness and refractive index in the surface forces apparatus (SFA), was used to measure spatial refractive index profiles.[30] An inverted microscope was used to focus white light on the device from above. The semi-reflective surfaces allow for constructive and deconstructive interference within the device, and the transmitted light was focused onto a spectrometer slit with a microscope objective (Fig. 1). The spectrometer (Shamrock series 300, 600 lines/mm grating) was connected to the outlet of the microscope and a CCD camera (Andor Luca-R) was used to gather images from the spectrometer (Fig. 2a). The horizontal axis in each image corresponds to the physical dimension in which light is obtained in

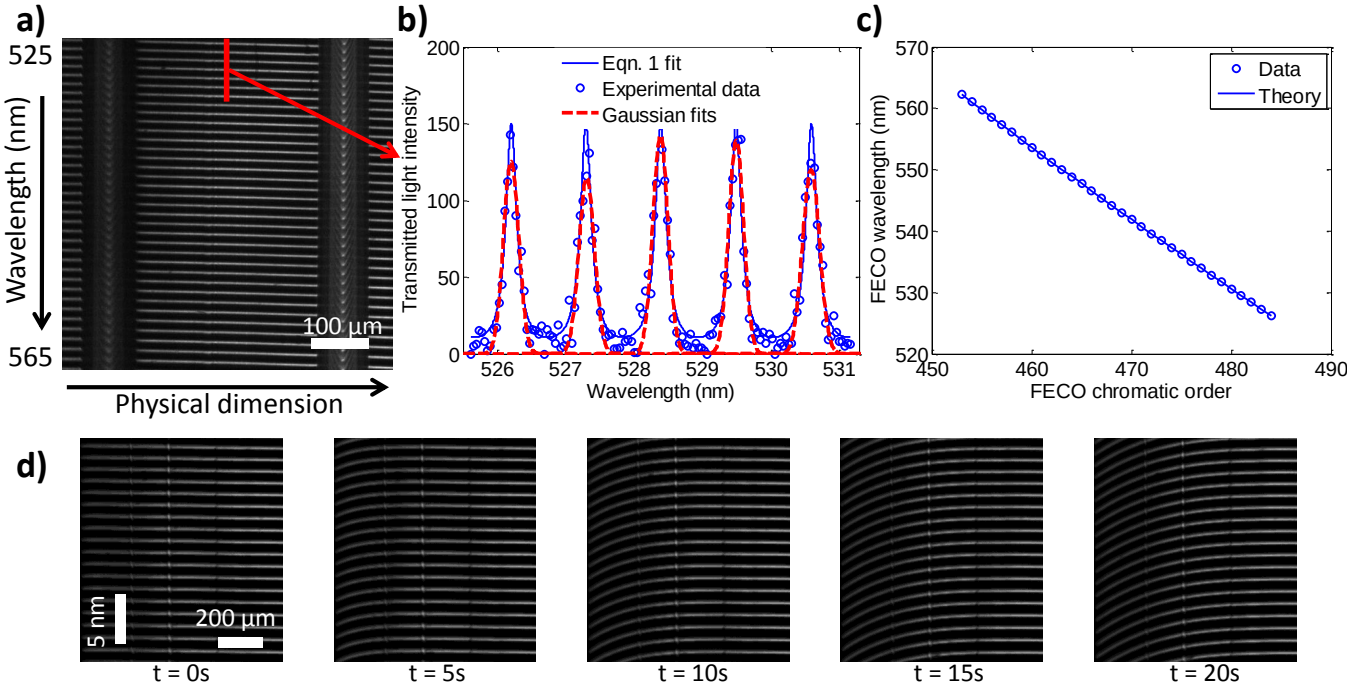

Fig. 2 (a) Image of FECO fringes generated with microfluidic chip (see Fig. 5 for image of microfluidic chip). (b) Light intensity profile (taken at position shown in (a)) as a function of wavelength demonstrating Gaussian fitting to FECO fringe locations. (c) Wavelength of FECO fringes from (a) as a function of chromatic order fit to Eqn 2. (d) Shift in FECO fringe location due to diffusion of ethanol from the left (See Fig. 4 for image of microfluidic chip).

the slit, while the vertical axis corresponds to the wavelength of diffracted light.

Due to the superposition of light waves which are reflecting between the two semi-reflective surfaces, the intensity of transmitted light though the interferometer is dependent on wavelength and the optical path. The intensity of transmitted light (I_t) through a one-layer multiple beam interferometer can be related to the intensity of normal incident light (I_0) via the Airy Function[31]:

$$I_t = I_0 \left[\frac{1}{1 + (\frac{2r}{1-r^2})^2 \sin^2(\frac{2\pi nd}{\lambda})} \right] \quad (1)$$

where n is the refractive index of the layer, r the reflection coefficient of the mirrors, d the distance between the two reflective surfaces, and λ the wavelength of the incident light. Fringes are observed at wavelengths of light which produce a maximum in transmitted light:

$$\lambda_m^F = \frac{2nd}{m} \quad (2)$$

where m represents the chromatic order of the fringe. The refractive index can be determined from Eqn. 2 with the distance between the reflective surfaces and the wavelengths of two *Fringes of Equal Chromatic Order* (FECO) with unknown successive chromatic orders m and $m+1$:

$$n = \left(\frac{1}{2d}\right) \frac{\lambda_m^F \lambda_{m+1}^F}{\lambda_m^F - \lambda_{m+1}^F}. \quad (3)$$

Although the thickness of the microfluidic channel is not known with high precision, the absolute refractive index can still be determined with Eqn. 3. The thickness of the channel can be calculated by calibrating with a liquid of known refractive index. Using this method, the error in a refractive index measurement (δn) scales with the error in the measurement of FECO fringe wavelength ($\delta\lambda$) with $\frac{\delta n}{n} \sim (\frac{d}{\lambda})(\frac{\delta\lambda}{\lambda})$. Here, the error in measuring the wavelength of a fringe is approximately limited by the resolution of the spectrometer and camera ($\delta\lambda \sim 0.05\,nm$), giving a refractive index precision of approximately $10^{-2}\,RIU$.

In order to measure small changes in concentration, a much greater precision in refractive index is required. Relative shifts in refractive index over time (t_0 to t) can be determined with higher precision than the absolute refractive index, by using Eqn. 2 to track the relative shift of individual fringes:

$$n(t) = n(t_0) \frac{\lambda_m^F(t)}{\lambda_m^F(t_0)}. \quad (4)$$

Here, knowledge of the initial refractive index is required, but no calibration is needed. With this method, the error in the measurement of refractive index scales with $\frac{\delta n}{n} \sim (\frac{\delta \lambda}{\lambda})$. Therefore, the refractive index can be determined with a precision of approximately $10^{-4} RIU$ (a subpixel method improves the precision to $2 \times 10^{-5} RIU$). It is interesting to note that the thickness of the channel does not affect the precision; however, there are limitations on channel thickness. A channel taller than $\sim 1mm$ makes it difficult to resolve individual fringes, while a channel shorter than ∼wavelength of light will not produce any fringes.

2.3 FECO fringe acquisition

Refractive index profiles were determined using Eqn. 4. The initial refractive index of the system was known for each experiment; therefore, only the peak wavelength of a FECO fringe is required to determine dynamic refractive index profiles. Images of the interferometric patterns were acquired at each time step, and the wavelengths of FECO fringes were tracked over time with image analysis.

The wavelength-dependent, transmitted light intensity profile was measured for each horizontal pixel, which corresponds to a specific point in space. A custom-written MATLAB code located the initial location of FECO fringes by finding the location of local light maxima. Improved resolution for the FECO fringe locations was then obtained by approximating the Airy Function (Eqn. 1) as a series of Gaussian peaks (Fig. 2b). To verify that FECO fringes are being observed, the wavelengths of the fringes from Fig. 2b are plotted against successive chromatic orders (Fig. 2c), and found to agree with Eqn 2.

After identifying the initial location of the FECO fringes, the fringes were tracked at each point in space and time. Averaging the relative shift in wavelength of at least 5 fringes, a spatio-temporal refractive index profile was calculated by applying Eqn. 4. Refractive index profiles were then converted to concentration profiles using previously measured refractive index data in the *CRC Handbook* .[32] Fig. 2d shows example FECO fringes shifting due to diffusion of ethanol.

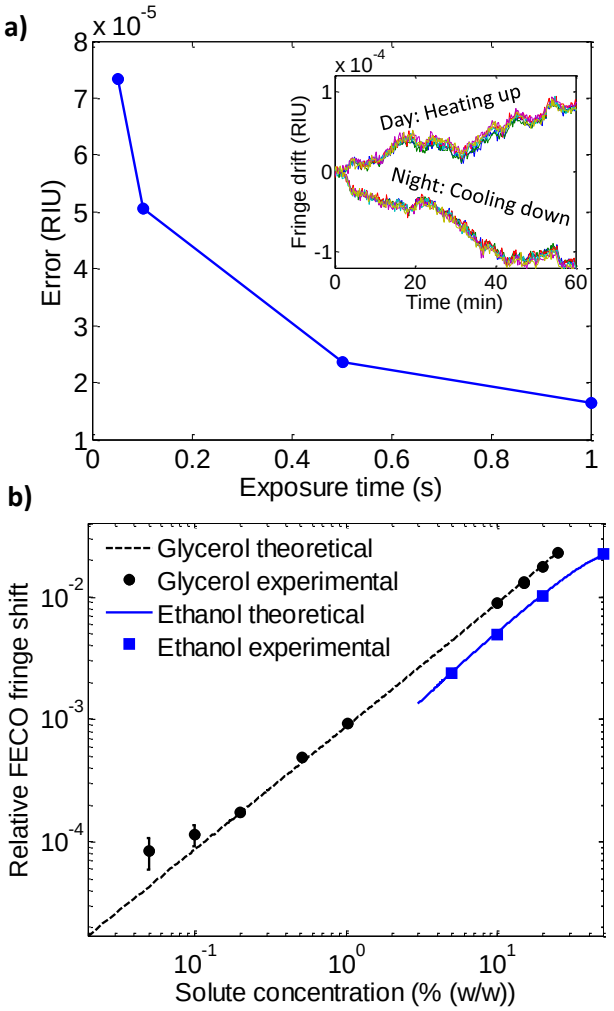

Fig. 3 (a) Error in refractive index measurement over 30 frames in a rectangular channel with water. Data is expressed as the standard deviation of the average relative fringe shift (averaged over 5 fringes). (Inset) Example drifts in the refractive index measurements of water due to temperature fluctuations. Colors represent 5 different positions across the channel. (b) Experimental fringe shifts when switching from water to solute with a defined concentration compared to theoretical switch predicted with Eqn 4 and refractive index data.[32] Data is expressed as mean ± SD (n = 20 fringes).

3 Characterization of technique

We now discuss the precision, accuracy, and resolution of measuring changes in refractive index. Fundamentally, the interferometry method is limited by the ability to precisely detect the position of the FECO fringes. Here, the accuracy and precision of the technique is independent of the distance between the two reflective surfaces as long as the refractive index is homogenous in the optical path. Although no calibration is required, the initial refractive index must be known to determine the refractive index at a later time.

The noise associated with a refractive index measurement is proportional to the relative noise associated in identifying a fringe wavelength. When imaging with the camera and spectrometer grating previously described, each pixel corresponds to a wavelength of $0.04\,nm$. A FECO fringe shift of $0.04\,nm$ corresponds to a shift of $\sim 10^{-4}$ RIU in water. By fitting each fringe with a Gaussian function and averaging relative shifts in wavelength over multiple fringes, we obtain sub-pixel resolution.

To estimate the precision of fringe detection, static images of pure water were taken. The error in fringe position was determined by finding the standard deviation of the average difference between each fringe position and the respective mean fringe position, averaged over 5 fringes. For long exposure times ($> 1s$), the refractive index shift precision plateaus at 1.8×10^{-5} RIU (Fig. 3a). When the exposure time is reduced, the signal to noise ratio decreases, decreasing the precision of the technique (Fig. 3a). However, even with an exposure time as short as 50 ms, the precision in refractive index remained less than 10^{-4} RIU, indicating that transient processes with time scales of 50 ms can be tracked.

Small measurement drifts are observed during long experiments (> 10 min). To quantify the drift, the refractive index of flowing water and stagnant air was measured over a day, at multiple positions in a microfluidic channel. The measurement can homogeneously increase or decrease up to $\sim 10^{-4}$ RIU/h during the day and night, respectively, throughout the microfluidic channel (Fig. 3a, inset). These observations suggest that the drift is due to temperature fluctuations leading to expansion/compression of the whole tape layer. For this paper, all measurements were taken within 10 min and the drift was negligible; however, the small drift can be corrected for by measuring the refractive index of a static solution during the course of the experiment.

The spatial resolution of the technique depends on the objective. With a 4x objective, the pixel size gives a spatial resolution of 1.91μm. As with all light microscopy applications, the spatial resolution is limited by diffraction, placing a limit of $\sim 1\mu$m on the spatial resolution.

To confirm the accuracy of the technique, fringe positions were tracked while changing the refractive index of a solution in a rectangular channel by switching from pure water to a homogenous mixture of glycerol or ethanol (Fig. 3b). The measured refractive index shift agrees with literature for refractive index shifts greater than that of $0.05\%(w/w)$ glycerol.[32] This is consistent with the previously measured precision (Fig. 3a). Furthermore, we studied the reproducibility of the method by measuring the refractive index shift from water to glycerol with three repeat trials per microchip on multiple chips. The error of the measured refractive index shifts between trials on one device and between different devices (2×10^{-5} RIU) is the same as the precision of the technique, indicating excellent reproducibility.

Measurement improvements are possible for both refractive index and temporal resolution. The location of each FECO fringe can be found with higher precision by increasing the resolution of the spectrometer grating or the camera, allowing for a smaller shift in the fringe to be measured. The combination of a faster camera and a brighter light source can improve the temporal resolution of the technique by lowering the required exposure time to detect FECO fringes.

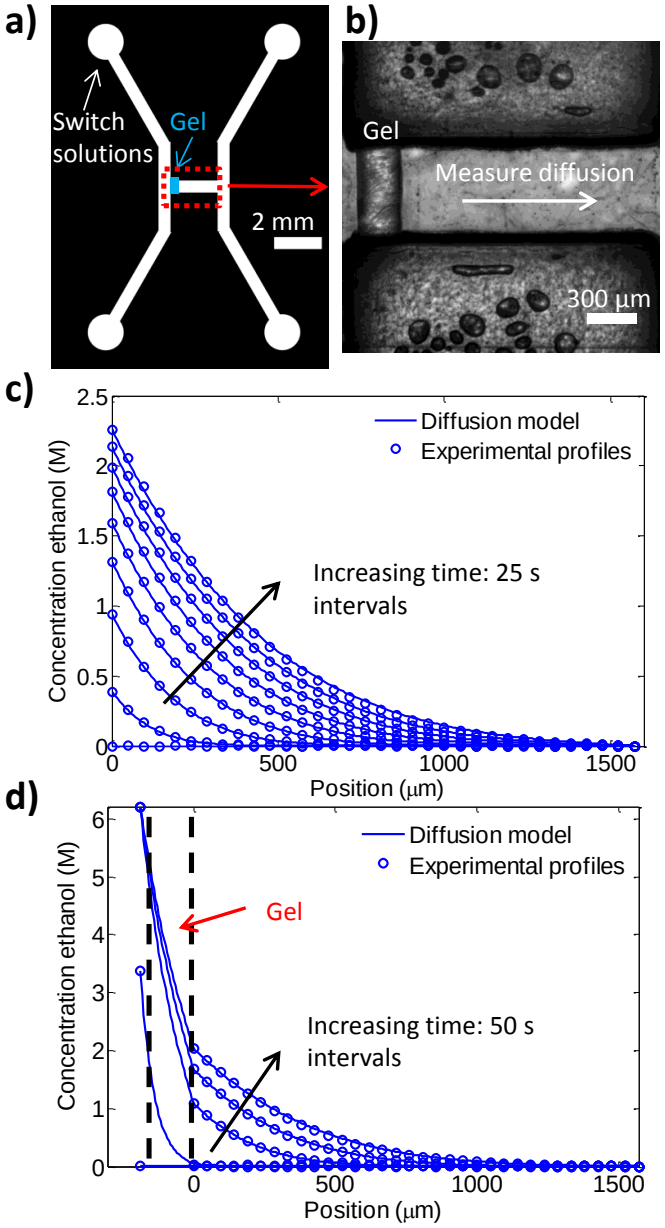

Fig. 4 (a) Microfluidic channel geometry for diffusivity measurements. (b) Microscopic image of photopolymerized PEG-DA gel and region for diffusivity measurements. (c) Experimentally measured evolution of glycerol diffusive front compared to numerical diffusion model. (d) Extraction of effective diffusivity in PEG-DA hydrogels with numerical model.

4 Measurement of binary diffusion coefficients

We now use the interferometer to monitor the diffusive evolution of chemical gradients. Experimental techniques used to generate and measure the chemical gradients are discussed. A numerical model is then compared to the experimental data to

Table 1 Literature and experimentally measured binary diffusivity in water D_0, concentration dependent factor b (Eqn. 6), and effective diffusivity parameter k in PEG-DA hydrogels (Eqn. 7).

	Literature values		Measured values		Measured values
Species	$D_0 \times 10^5$ / (cm^2/s)	b / $(1/M)$	$D_0 \times 10^5$ / (cm^2/s)	b / $(1/M)$	k
Glycerol	0.99 [33]	0.08 [33]	0.90 ± 0.05	0.26 ± 0.07	0.22 ± 0.03
Ethanol	1.24 [34]	0.10 [34]	1.21 ± 0.05	0.12 ± 0.02	0.34 ± 0.02
2-propanol	1.01 [35]	0.17 [35]	1.04 ± 0.02	0.23 ± 0.02	0.15 ± 0.01
Sucrose	0.52 [36,37]	0.40 [36,37]	0.52 ± 0.31	2.4 ± 0.5	0.29 ± 0.02
Glucose	0.67 [38]	0.36 [38]	0.59 ± 0.03	0.8 ± 0.3	0.19 ± 0.02
	w = 0-30% (w/w) , T = 298 K		w = 0-10% (w/w), T=296 $\pm$ 1 K		w = 0-30% (w/w), T=296 $\pm$ 1 K

extract binary diffusivities in both free solution and PEG-DA hydrogels.

4.1 Experimental design

A microfluidic chip, allowing for the semi-infinite propagation of a diffusive front was fabricated as shown in Fig. 4a. PEG-DA hydrogels are used to isolate channels with flow from stagnant channels. [12] The hydrogels allow for the generation of diffusive chemical gradients, by being permeable to diffusive transport but impermeable to convection.

The PEG-DA hydrogels were polymerized *in situ* using microscope projection lithography. [12] The aqueous precursor solution consisted of 40% (v/v) PEG-DA-DA 600 (n=400, Polysciences Inc.) and 5% (v/v) photoinitiator (2-hydroxy-2methylpropiophenone, Sigma Aldrich), and was exposed with 40 mW ultraviolent light through a 500 μm slit with a 10x objective for 500 ms. Here, the width of the PEG-DA hydrogels are much wider than those made by *Paustian et al.*; however, thinner gels could have been fabricated to allow for faster diffusive switching. [12]

4.2 Diffusivity measurements in water

To measure binary diffusivities in water, the device was initially filled completely with water, and flow to the measurement region was stopped with tubing clamps. By changing inlet tubing, flow to the side channel was switched from water to various solutes at 30% (w/w). After performing the chemical switch, interferometry was used to track the evolution of the chemical gradient (Fig. 4b). Images of the interferometry pattern were acquired with 1s exposure time, and FECO fringe displacements were tracked over time to determine the relative shift in refractive index as a function of position. The refractive index shifts were then converted to concentrations using Eqn. 4, the known initial concentration, and concentration versus refractive index data. [32]

Least squares regression and a numerical diffusion model (Eqn. 5) were used to extract diffusivities and their concentration dependence. A linear relationship between concentration and diffusivity was assumed based on the solutes and concentration ranges used in the study (Eqn 6). [33–38]

$$\frac{\partial C(x,t)}{\partial t} = \frac{\partial}{\partial x}\left(D(C(x,t))\frac{\partial C(x,t)}{\partial x}\right) \quad (5)$$

$$D(C) = D_0(1 - bC) \quad (6)$$

One boundary condition was provided by the measured concentration just outside the hydrogel, while the concentration at the far end remained zero during each experiment. Dilute diffusivities (D_0) were extracted at early times of the chemical switch at low concentrations, while the concentration dependence on diffusivity (b) was extracted from the entire time course of the experiment.

The numerical model, with best fit diffusivity values, shows strong agreement with the experimentally measured concentration profiles, as seen for ethanol in Fig. 4c. This measurement was repeated at least 5 times, on 2 different microchips, for various solutes, and the best fit values are shown in Table 1. The measured values of the dilute diffusivity agree with previously published literature values for all solutes. [33–38] Measurements of b agree well with literature values for ethanol and 2-propanol; [34,35] however, they are higher than literature values for glucose, glycerol, and sucrose. [33,36–38] In the literature, the diffusion coefficients are measured with very small chemical gradients centered at different concentrations, while we extract the concentration dependence from a single steep chemical gradient. We believe the discrepancy for glucose, glycerol, and sucrose is due to the difference in measurement technique; however, this is still under investigation.

Compared to current diffusivity measurement techniques, our method has many benefits. Small diffusive length scales enable diffusivities to be measured with less than 5% variability in minutes. In addition, because concentration profiles are spatially resolved, subtle effects, such as diffusivity changes with concentration, can be measured with the technique.

4.3 Transport through the PEG-DA hydrogels

Although the FECO fringes are difficult to resolve within the hydrogel, the numerical model can be extended to include transport through the hydrogels. The effective diffusion coefficient in the hydrogel was assumed to be proportional to the free solution diffusion coefficient (with parameter k), independent of concentration:

$$D_{gel}(C) = k \times D_{sol}(C). \quad (7)$$

Boundary conditions were measured experimentally and the effective diffusivity in the hydrogel was found with least squares regression. The free solution diffusivity was taken from literature reports (Table 1), because concentrations in the gel were much higher than the concentration range in which free solution diffusivities were determined in this study. The numerical model shows strong agreement with the experimental data, as shown for ethanol in Fig. 4d. Effective diffusivities within PEG-DA range from 0.15 to 0.35 times the free solution diffusivity for the solutes tested (Table 1).

5 Evolution of a chemical gradient in a CDC

Multiple transport processes contribute to the development of concentration fields in CDCs. The chemical species must diffuse through both the hydrogels and the CDC to fully develop a steady state concentration profile. Within the gel, the diffusive resistance can vary significantly from free solution due to physical effects, such as size exclusion, or chemical effects, such as partitioning.[39] In addition, the constant diffusion coefficient assumption may fail when working with concentrated solute mixtures. We now use the technique to measure the generation of a chemical gradient in a CDC directly.

The CDC interferometer consists of three channels, which are connected within a central region, where the CDC is located (Fig. 5a). Photopolymerized hydrogels form the CDC (Fig. 5b).[12] For all experiments, all three channels were initially filled with a homogenous solute mixture, with a known concentration. After establishing homogenous conditions throughout the device, flow was stopped to the center CDC channel with external valves. New solute mixtures were flowed through the exterior channels to generate a chemical gradient across the CDC. The chemical switches were performed by manually changing external, inlet tubing.

For the diffusion studies presented here, all three channels were initially filled with an average solute mixture, and fluids in the two reservoir channels were replaced with pure water and a solution with twice the average concentration, respectively. By initially filling the device with an average solute mixture, the amount of transverse diffusion into the center channel is significantly reduced. In addition, the length scale required for diffusion is halved, reducing the time required to reach steady state by 75%.

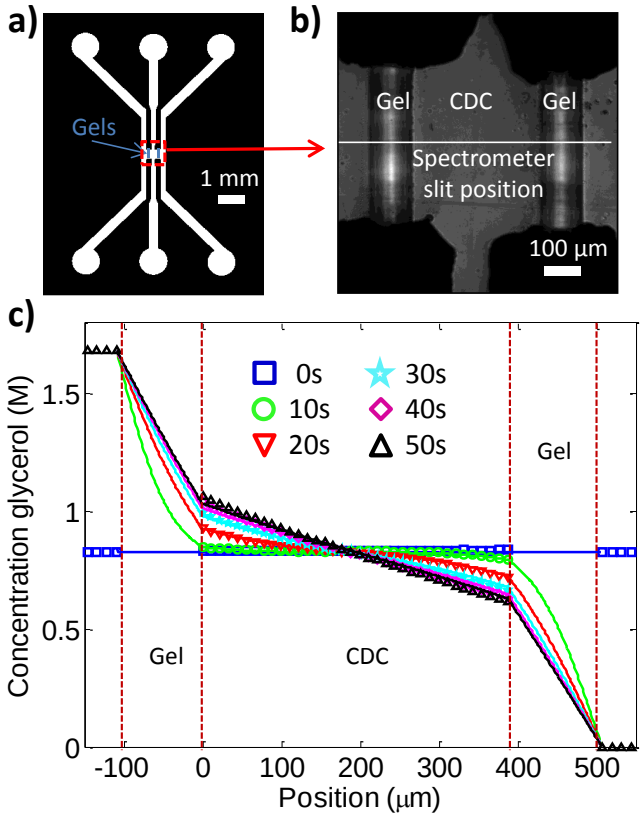

Fig. 5 (a) Dimensions of microfluidic chip containing CDC and PEG-DA hydrogels. (b) Microscopic image of CDC showing spectrometer slit position. (c) Best fit numerical model using Eqns. 5-7 (lines) agrees with experimental data (shapes).

FECO interferometry was used to track concentration profiles within the CDC and in the side control channels. The spectrometer slit was positioned perpendicular to the PEG-DA hydrogels in the center of the CDC (Fig. 5b), generating fringe patterns similar to those shown in Fig. 2a. An example experiment displaying the measurement of gradient generation is shown in Fig. 5c. Concentration profiles were not measured within the PEG-DA hydrogels because FECO fringes are not easily resolved.

The 1D diffusion model (Eqns. 5-7) and diffusivity measurements (Table 1) were compared to the measured concentration fields in the CDC. The model accurately predicts the evolution of the chemical concentration profile, as demonstrated for glycerol in Fig. 5c. Excellent agreement is also observed between the numerical model and experimental data within the CDC for other glycerol concentrations and for the other solutes tested (ethanol, isopropanol, glucose, and sucrose). Based on the diffusivity measurements shown in Ta-

ble 1, many features of the steady state profile observed in the CDC (Fig. 5c) could have been predicted. First, the concentration drop across the hydrogels is three times greater than the water equivalent due to the lower diffusivity. In addition, the steady state concentration profile is not completely linear due to the concentration dependent diffusivity. Notably, the concentration in the center of the CDC differs slightly from the average concentration of the two side channels.

6 Conclusions

We have developed a novel interferometry method to measure concentration fields *in situ* in microfluidic devices, without any fluorescent labeling. The technique requires very simple fabrication steps, and it easy to set up using equipment that is standard in many research laboratories. The refractometry method has good spatial and temporal resolutions (1 μm and 50 ms, respectively) with a refractive index sensitivity of 10^{-5} RIU. Here, we have used the technique to quickly measure binary diffusivities with high precision (less than 5 % error), and extract both the concentration dependence on diffusivity and effective diffusivity in PEG-DA hydrogels. The technique was also applied to directly measure the generation of a chemical gradient in a CDC.

Although the ability to resolve changes in refractive index down to 10^{-5} RIU is not new, as other microfluidic interferometry geometries have resolved changes down to 10^{-7} RIU,[25] the ability to resolve these changes in both space and time makes the technique a useful and novel tool. We anticipate our technique will prove useful for directly measuring and visualizing spatio-temporal concentration profiles, opening new possibilities for the direct interrogation of materials and systems as they equilibrate, react, dissolve, or crystallize.

Acknowledgments

This work was supported by the NSF under Grant CBET-1438779 and the NSF Graduate Research Fellowship under Grant DGE-1144085 (D.R.V. and M.R.), with additional support from the Dow Chemical Company through the Dow Materials Institute at the University of California, Santa Barbara (UCSB). The authors also acknowledge the Jacob Israelachvili lab for assistance with preliminary studies. Work was performed in UCSB's Materials Research Laboratory Central Facilities, which are supported by the NSF Materials Research Science and Engineering Centers Program under Grant DMR05-20415, a member of the NSF-funded Materials Research Facilities Network, and in the UCSB nanofabrication facility, part of the NSF-funded National Nanotechnology Infrastructure Network.

References

1 T. Ahmed, T. S. Shimizu and R. Stocker, *Nano letters*, 2010, **10**, 3379–85.
2 N. Li Jeon, H. Baskaran, S. K. W. Dertinger, G. M. Whitesides, L. Van de Water and M. Toner, *Nature biotechnology*, 2002, **20**, 826–30.
3 P. J. Hung, P. J. Lee, P. Sabounchi, N. Aghdam, R. Lin and L. P. Lee, *Lab on a chip*, 2005, **5**, 44–8.
4 H.-J. Koo, K. V. Waynant, C. Zhang and P. V. Braun, *ACS applied materials & interfaces*, 2014.
5 X. Zhang, X. Gao, L. Jiang and J. Qin, *Langmuir : the ACS journal of surfaces and colloids*, 2012, **28**, 10026–32.
6 J. N. L. Albert, T. D. Bogart, R. L. Lewis, K. L. Beers, M. J. Fasolka, J. B. Hutchison, B. D. Vogt and T. H. Epps, *Nano letters*, 2011, **11**, 1351–7.
7 N. L. Jeon, S. K. W. Dertinger, D. T. Chiu, I. S. Choi, A. D. Stroock and G. M. Whitesides, *Langmuir*, 2000, **16**, 8311–8316.
8 S. K. W. Dertinger, D. T. Chiu, N. L. Jeon and G. M. Whitesides, *Analytical Chemistry*, 2001, **73**, 1240–1246.
9 D. Ahmed, C. Y. Chan, S.-C. S. Lin, H. S. Muddana, N. Nama, S. J. Benkovic and T. J. Huang, *Lab on a chip*, 2013, **13**, 328–31.
10 D. C.-W. Tan, L.-Y. L. Yung and P. Roy, *Biomedical microdevices*, 2010, **12**, 523–32.
11 E. Choi, H.-k. Chang, C. Y. Lim, T. Kim and J. Park, *Lab on a chip*, 2012, **12**, 3968–75.
12 J. S. Paustian, R. N. Azevedo, S.-T. B. Lundin, M. J. Gilkey and T. M. Squires, *Physical Review X*, 2013, **3**, 041010.
13 J. Palacci, C. Cottin-Bizonne, C. Ybert and L. Bocquet, *Soft Matter*, 2012, **8**, 980–994.
14 J. J. VanDersarl, A. M. Xu and N. a. Melosh, *Lab on a chip*, 2011, **11**, 3057–63.
15 S.-Y. Cheng, S. Heilman, M. Wasserman, S. Archer, M. L. Shuler and M. Wu, *Lab on a Chip*, 2007, **7**, 763–9.
16 J. Diao, L. Young, S. Kim, E. a. Fogarty, S. M. Heilman, P. Zhou, M. L. Shuler, M. Wu and M. P. DeLisa, *Lab on a Chip*, 2006, **6**, 381–8.
17 A. M. Tentori and A. E. Herr, *Journal of micromechanics and microengineering : structures, devices, and systems*, 2011, **21**, 54001.
18 S. E. Barnes, Z. T. Cygan, J. K. Yates, K. L. Beers and E. J. Amis, *The Analyst*, 2006, **131**, 1027–33.
19 L. Daubersies, J. Leng and J.-B. Salmon, *Soft Matter*, 2012, **8**, 5923–32.
20 L. Daubersies, J. Leng and J.-B. Salmon, *Lab on a chip*, 2013, **13**, 910–9.
21 K. L. A. Chan and S. G. Kazarian, *Analytical chemistry*, 2012, **84**, 4052–6.
22 D. Schafer, J. A. Squier, J. van Maarseveen, D. Bonn, M. Bonn and M. Müller, *Journal of the American Chemical Society*, 2008, **130**, 11592–3.
23 A. Crespi, Y. Gu, B. Ngamsom, H. J. W. M. Hoekstra, C. Dongre, M. Pollnau, R. Ramponi, H. H. van den Vlekkert, P. Watts, G. Cerullo and R. Osellame, *Lab on a chip*, 2010, **10**, 1167–73.
24 D. J. Bornhop, J. C. Latham, A. Kussrow, D. a. Markov, R. D. Jones and H. S. Sø rensen, *Science (New York, N.Y.)*, 2007, **317**, 1732–6.
25 a. Ymeti, J. S. Kanger, J. Greve, G. a. J. Besselink, P. V. Lambeck, R. Wijn and R. G. Heideman, *Biosensors & bioelectronics*, 2005, **20**, 1417–21.
26 H. Shao, D. Kumar, S. Feld and K. Lear, *Journal of Microelectomechanical Systems*, 2005, **14**, 756–762.
27 G. Gervinskas, P. Trocha, R. Buividas, D. J. Day, E. Scheer, P. Leiderer and S. Juodkazis, Smart Nano-Micro Materials and Devices, 2011, p. 82043Q.
28 J. Tian, Y. Lu, Q. Zhang and M. Han, *Optics express*, 2013, **21**, 6633–9.
29 K. M. van Delft, J. C. T. Eijkel, D. Mijatovic, T. S. Druzhinina, H. Rathgen, N. R. Tas, A. van den Berg and F. Mugele, *Nano letters*, 2007, **7**, 345–50.
30 J. Israelachvili, *Journal of Colloid and Interface Science*, 1973, **44**, 259–272.

31 P. Hariharan, *Basics of interferometry*, Elsevier, Burlington, MA, 2nd edn., 2007, p. 134.

32 *CRC Handbook of Chemistry and Physics, 85th Edition*, ed. D. R. Lide, 2004.

33 G. Ternström, A. Sjöstrand, G. Aly and A. Jernqvist, *Journal of Chemical & Engineering Data*, 1996, **41**, 876–879.

34 K. Pratt and W. Wakeham, *Proceedings of the Royal Society London*, 1974, **336**, 393–406.

35 K. Pratt and W. Wakeham, *Proceedings of the Royal Society London*, 1975, **342**, 401–419.

36 A. C. F. Ribeiro, O. Ortona, S. M. N. Simões, C. I. A. V. Santos, P. M. R. A. Prazeres, A. J. M. Valente, V. M. M. Lobo and H. D. Burrows, *Journal of Chemical & Engineering Data*, 2006, **51**, 1836–1840.

37 P. Henrion, *Trans. Faraday Soc.*, 1964, **60**, 72–4.

38 M. Castaldi, G. D'Errico, L. Paduano and V. Vitagliano, *Journal of Chemical & Engineering Data*, 1998, **43**, 653–657.

39 E. Cussler, *Diffusion: Mass transfer in fluid systems*, Cambridge University Press, New York, NY, 1984.